Combining Thickness Information with Surface

Tensor-based Morphometry for the 3D

Statistical Analysis of the Corpus Callosum

by

Liang Xu

A Thesis Presented in Partial Fulfillment
of the Requirements for the Degree
Master of Science

Approved November 2013 by the
Graduate Supervisory Committee:

Yalin Wang, Chair
Ross Maciejewski
Jieping Ye

ARIZONA STATE UNIVERSITY

December 2013

ABSTRACT

In blindness research, the corpus callosum (CC) is the most frequently studied sub-cortical structure, due to its important involvement in visual processing. While most callosal analyses from brain structural magnetic resonance images (MRI) are limited to the 2D mid-sagittal slice, we propose a novel framework to capture a complete set of 3D morphological differences in the corpus callosum between two groups of subjects. The CCs are segmented from whole brain T1-weighted MRI and modeled as 3D tetrahedral meshes. The callosal surface is divided into superior and inferior patches on which we compute a volumetric harmonic field by solving the Laplace's equation with Dirichlet boundary conditions. We adopt a refined tetrahedral mesh to compute the Laplacian operator, so our computation can achieve sub-voxel accuracy. Thickness is estimated by tracing the streamlines in the harmonic field. We combine areal changes found using surface tensor-based morphometry and thickness information into a vector at each vertex to be used as a metric for the statistical analysis. Group differences are assessed on this combined measure through Hotelling's T2 test. The method is applied to statistically compare three groups consisting of: congenitally blind (CB), late blind (LB; onset > 8 years old) and sighted (SC) subjects. Our results reveal significant differences in several regions of the CC between both blind groups and the sighted groups; and to a lesser extent between the LB and CB groups. These results demonstrate the crucial role of visual deprivation during the developmental period in reshaping the structural architecture of the CC.

To my loved ones for all the encouragement

TABLE OF CONTENTS

LIST OF FIGURES

LIST OF SYMBOLS / NOMENCLATURE

Symbol   Page

INTRODUCTION

Medical Background

Of the 119 million people in the United States who are age 40 and over, 3.4 million are visually impaired or blind. Worldwide, about 160 million people are similarly affected. Fortunately, new technologies such as corneal and retinal implants are emerging that have the potential to restore vision (Sieving et al., 2006; Belluck, 2013). However, the effects of rehabilitation therapies may vary with age of onset of blindness, as visual cognitive areas may have been recruited by other senses, particularly in subjects who became blind at younger ages. Additionally, prior work (Voss et al., 2004; Doucet et al., 2006; Collignon et al., 2007; Gougoux et al., 2009) has demonstrated that understanding how sensory deprivation affects brain anatomy may help rehabilitation design in previously sensory deprived subjects for whom missing senses have been restored.

In combination with recent advances in the collection and data-basing of brain MRI, anatomical and functional MRI analyses methods have begun to shed light on blindness adaptation mechanisms (Amedi et al., 2003; Leporé et al., 2009; Jiang et al., 2009; Park et al., 2009; Leporé et al., 2010; Bedny et al., 2011; Ricciardi and Pietrini, 2011; Voss and Zatorre, 2012; Wang et al., 2013a; Bock et al., 2013). As a non-invasive and high-throughput analysis tool, neuroimaging can help better understand the neuroanatomical correlates of blindness, cross-modal plasticity and its relationship to age of onset and thus improve post- blindness rehabilitation efficacy. In addition to this important clinical application, the study of the brain architecture of blind individuals versus age of onset has the potential to provide important and groundbreaking new insights on the old "nature versus nurture" debate on the mind/brain development (Ricciardi and Pietrini, 2011).

1

For blindness research, the corpus callosum (CC) is a frequently studied subcortical structure in post-processing analyses of magnetic resonance images (Leporé et al., 2010; Bock et al., 2013). This is in part due to its deep involvement in visual processing in brain. The splenium of the CC carries fibers that connect visuo-spatial areas of the brain, and the isthmus is also involved in visuo-spatial processing, as it contains fibers connecting the posterior parietal areas, which fuse multimodality sensory information (Hofer and Frahm, 2006). The CC undergoes extensive myelinization during development until adolescence, and waves of peak growth rates can be observed in the CC's of children of different ages (Hua et al., 2009). Hence, studying the respective impact of congenitally (CB) versus lately acquired blindness (LB) on the anatomy of the CC provides a unique model to probe how experience at different developmental periods shapes the structural organization of the brain.

Related Work

On the processing side, in T1-weighted MRI, its high contrast difference from surrounding structures make accurate mid-sagittal callosal segmentations straightforward for both manual and automatic methods (Thompson et al., 2003; Styner et al., 2005b; Luders et al., 2006, 2010). Additionally, its functional differentiation along an elongated sagittal axis has allowed researchers to focus on 2D analysis of the mid-sagittal section, allowing for simpler and faster numerical tools, e.g. (Thompson et al., 2003; Luders et al., 2006, 2010; Tepest et al., 2010; Adamson et al., 2011; Di Paola et al., 2012; Herron et al., 2012). Even so, it is clear that a 3D structural analysis, which model CC morphometry with a continuous surface spanning over several image slices, can help visualization and may pick up some important information that is discarded by the single image slice processing.

2

We propose a novel geometric modeling pipeline for the analysis of the CC and apply it to study the influence of various ages of blindness onsets on the CC. while most studies have focused on 2D representations of this structure, our team (Wang et al., 2012b) compared surfaces generated from 3D CC in premature neonates to those of term-born controls. In that work, a surface grid was generated on the CC, and callosal thickness was computed as the distance from a medial axis. Statistical significance was assessed at each vertex on a vector containing the thickness and the deformation tensors from a multivariate tensor- based morphometry analysis (mTBM). The deformation tensors represent changes in area on the surface. However, for concave callosal surfaces, the medial axis is not well-defined and does not always have a biologically meaningful interpretation. Here we propose a new thickness computation to be combined with the standard mTBM analysis as in (Wang et al., 2012b). Given 3D tetrahedral meshes of the CC, we use the tetrahedral mesh based Laplacian operator to compute a harmonic field. We adopt the volumetric Laplacian operator proposed in our prior work (Wang et al., 2004a), which became the de facto standard for volumetric harmonic map research (Wang et al., 2004b; Li et al., 2007; Tan et al., 2010; Pai et al., 2011; Li et al., 2010; Paille and Poulin, 2012; Wang et al., 2012a; Xu et al., 2013; Li et al., 2013; Wang et al., 2013b). We extend our prior work and rigorously prove that the conventional harmonic energy is equivalent to the discrete harmonic energy on a tetrahedral mesh and one may use the discrete volumetric Laplacian operator to compute the harmonic field. The thickness is then computed from the streamlines of the harmonic field. The estimated callosal thickness is well-defined, and should reflect the intrinsic 3D geometrical structure better than thickness derived from a medial axis, and hence facilitates consistent cross-subject comparisons.

In the field of computational anatomy, tensor-based morphometry (TBM) (Davatzikos, 1996; Chung et al., 2001) and more recently its multivariate extension, mTBM (Leporé et al., 2008; Wang et al., 2011), have been used extensively to detect regional differences in surface and volume brain morphology between two groups of subjects. In surface mTBM, brain T1-weighted MRIs from two groups of subjects are registered to a common template, and a Jacobian matrix J is computed at each vertex from the registration between a template and each of the subject's images. The J s, or a function of their components, is used as metrics for group comparisons. Here we focus more specifically on mTBM on the callosal surface. Prior work (Wang et al., 2011) combining mTBM with other statistics such as the radial distance significantly improved statistical power. Intuitively, thickness and mTBM are complementary, as thickness describes distances roughly along the surface's normal direction, while mTBM detects surface dissimilarities, including differences in the surface metric tensor induced by the particular surface parameterization. So we propose that a combination of thickness and mTBM will offer a complete set of surface statistics for callosal morphometry and hypothesize that they may boost statistical power to detect disease effects compared to 2D mid-sagittal analyses.

Thesis Overview

In this paper, we propose a combined thickness/mTBM multivariate morphometry statistic to study callosal differences associated with congenital-onset versus late-onset blindness. Our pipeline is applied on a data set consisting of: 14 congenitally blind (CB), 10 late blind (LB; onset > 8 years old) and 20 sighted control (SC) subjects. Prior 2D TBM analyses of the corpus callosum (Leporé et al., 2010) revealed reductions in the isthmus and the splenium of the corpus callosum in early but not late blind compared to sighted controls. However, comparisons of the early and late blind groups did not find any significant changes. Additionally, (Leporé

et al., 2010) observed changes in the frontal lobes, though those were not reflected in the 2D analyses of the genu of the CC. Here we set out to test our whether additional subtle blindness related changes may be detected by our more powerful method.
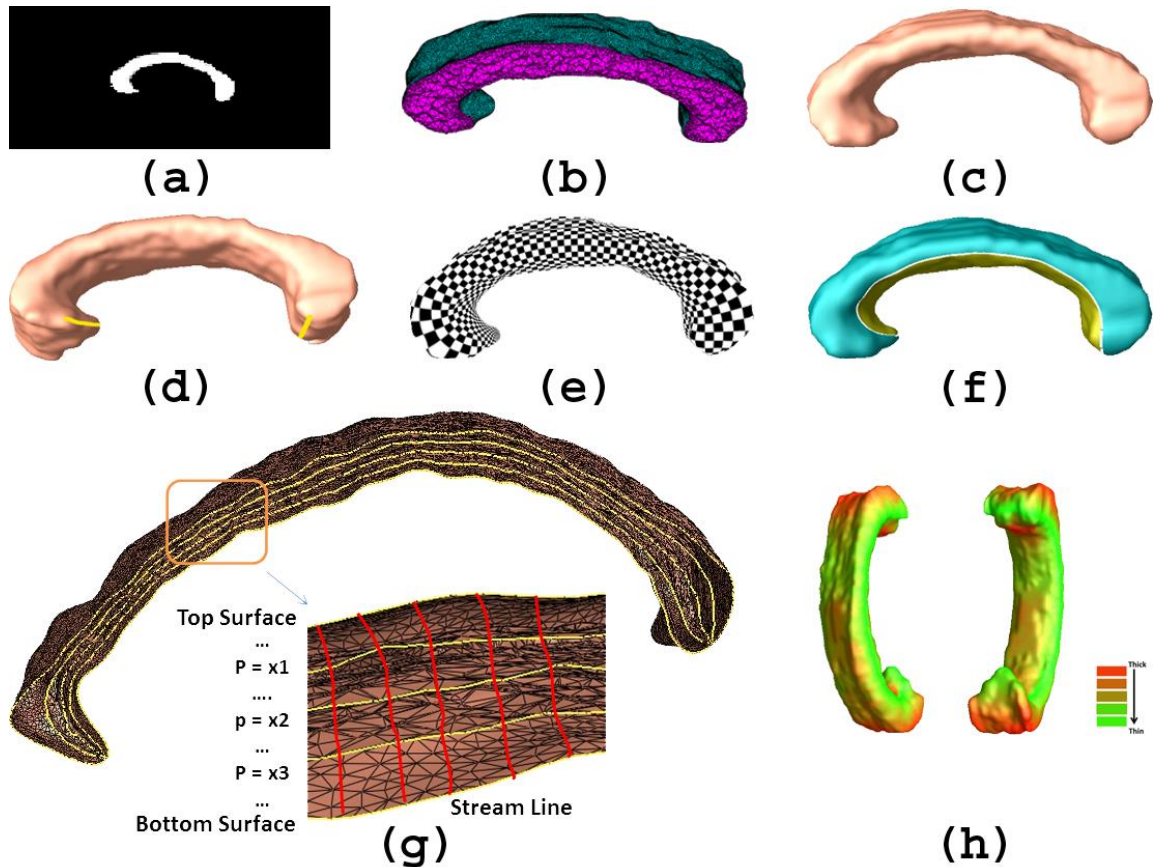
Figure 1. Algorithm pipeline illustrated by intermediate results

Figure 1 summarizes our overall sequence of steps used to analyze corpus callosum morphometry. First, we manually segment callosal contours (a). We model each of the CC with a tetrahedral mesh (b) with a triangle surface as it boundary (c). Then we apply our in-house conformal mapping and constrained harmonic map methods (Wang et al., 2010) to register callosal surfaces across all subjects ((d) and (e)). In (f), the registered surface is decomposed into two parts: superior (blue) and inferior (yellow) part. To estimate callosal thickness, the volumetric Laplace Beltrami

5

coefficients are used to solve the Laplace's equation and the thickness is measured by the stream line lengths between superior and inferior parts (g). And (h) shows us the thickness color map on callosal surface: the red color means thick and the green color means thin. Last, multivariate statistics including thickness and multivariate tensor-based morphometry (mTBM) (Wang et al., 2010) are applied to identify regions with significant differences between any two of our three groups. False discovery rate (FDR) is used to assign global (corrected) p-values for effects seen in surface based statistical.

SUBJECTS AND PREPROCESSING

Data Acquisition

Subjects with no history of neurological, cognitive or sensorimotor deficits other than blindness participated in the study and were divided into two groups. The first group consisted of 14 congenitally blind individuals, aged between 16 and 61 years (10 men, 4women). The second group consisted of 10 late-onset blind subjects (i.e., with loss of vision more than 8 years) aged between 42 and 60 years (3 men, 7 women). Each of these groups was compared with a healthy group of 20 controls (9 males, 11 females). Figure 2 lists the detailed of age, gender and blindness duration information for these three groups. In all cases, blindness was attributable to bilateral peripheral damage (including: lenticular fibroplasia, retinoblastoma, tumors restricted to the eyes, retinal detachment, Leber's congenital amaurosis, retinas pigmentosa, accidents affecting the eyes and glaucoma) and led to total blindness. For brevity, we refer to congenitally and late-onset blind subjects as CB and LB for the rest of the paper.

		CB	LB	SC
Age	Range	26 - 61	42 - 60	23 – 60
	Average	42.64	51.60	38.30
	S.D.	11.35	5.56	13.48
Gender	Male	10	3	9
	Female	4	7	11
Years of Blindness	Average	42.64	26.90	-
	S.D.	11.39	16.61	-
Years of Total Blindness	Average	42.64	13.00	-
	S.D.	11.39	10.25	-

Figure 2. Detailed information for all subjects

The research protocol was approved by the ethics committees of the Center for Interdisciplinary Research in Rehabilitation, which coordinates research with blind subjects in the Province of Quebec. MRI scans were collected at the Centre Hospitalier de l'Université de Montreal (CHUM). All subjects provided written informed consent prior to testing.

For each participant, high-resolution volumetric MRI scans of the brain were acquired on a 3T MP-RAGE Siemens Tim Trio MRI Scanner (Siemens Electric, Erlangen, Germany). The scanning protocol was identical for all participants. Structural T1-weigthed 3D MPRAGE sequence (voxel size: $1 \times 1 \times 1.2$ mm3; matrix size: 240×256; slices: 160; sagittally-oriented MRI gradient echo sequence with repetition time (TR): 2300 ms; echo time (TE): 2.91 ms; inversion time (TI): 900 ms; and field of view (FoV): 256 mm) were acquired for each subject using the same scanner, equipped with a 12-channel head coil.

Preprocessing of Data

Coronal View   Sagittal View   Axial View
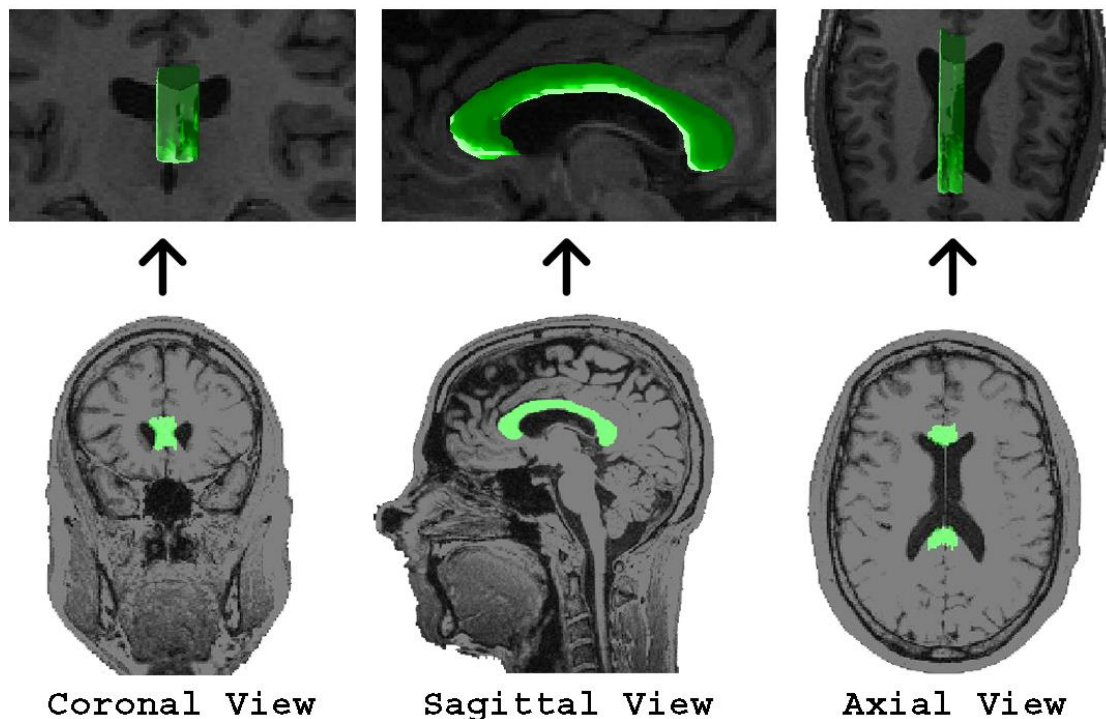
Figure 3. Corpus Callosum Segmentation Results

Images were aligned and scaled to the ICBM-53 brain template (International Consortium for Brain Mapping) with the FLIRT software (Jenkinson and Smith, 2001), using a 9-parameter linear transformations (3 translations, 3 rotations and 3 scales). We then manually segmented the CCs with Insight Toolkit's SNAP program (Yushkevich et al., 2006) as shown in Figure 3. Tracings were performed in the registered template space by a trained investigator (Y.K.) and the results were checked by an experienced neuroscientist (F.L.). We consulted neuroanatomical references of the corpus callosum to help guide the placement of the contours. The bottom row in Figure 3 shows the segmented CC contours overlaid on the MR image. The top row illustrates the built callosal surfaces overlaid on the MR images.

CALLOSAL THICKNESS ESTIMATION

In our pipeline, the callosal thickness is estimated by two steps. First, by solving Laplace's equation with volumetric Laplacian operators (Wang et al., 2004a), we build a harmonic field between superior and inferior callosal surfaces. It is followed by tracing the streamlines which are orthogonal to the equipotential surfaces in the computed harmonic field.

Solving Laplace's Equation

Laplace's equation $\Delta f = \nabla^2 f = 0$ in 3D Cartesian coordinates takes the form:

$$\left(\frac{\partial^2}{\partial x^2} + \frac{\partial^2}{\partial y^2} + \frac{\partial^2}{\partial z^2} \right) f(x, y, z) = 0 \tag{1}$$

f is called harmonic if it satisfies the Laplace's equation with Dirichlet boundary conditions. The computed function is called the harmonic field. Assume there are two boundaries, B_0 and B_1, the harmonic field is computed by solving for the harmonic function $f_M : M \rightarrow R$, such that

$$\begin{cases} \Delta f_M(p) = 0 & \forall_p \notin B_0 \cup B_1 \\ f_M(p) = 0 & \forall_p \in B_0 \\ f_M(p) = 1 & \forall_p \in B_1 \end{cases} \tag{2}$$

Equation 2 has been used to estimate the thickness of cerebral cortex (Jones et al., 2000; Schmitt and Bohme, 2002; Yezzi and Prince, 2003; Hutton et al., 2008) and CC thickness on the mid-sagittal section (Adamson et al., 2011). Here we propose a tetrahedral mesh based approach to solve Equation 2 and achieve sub-voxel accuracy on the boundaries. Compared with prior voxel-based schemes (Jones et al., 2000; Adamson et al., 2011; Schmitt and Bohme, 2002; Yezzi and Prince, 2003; Hutton et al., 2008), our new work has two major advantages. First, because the boundary of a tetrahedral mesh is a surface, our work can combine thickness estimation with the surface registration results so that one can achieve a comprehensive morphometry analysis by integrating CC thickness and surface area

change information. Secondly, a smooth surface may better model the CC structure boundaries, which may overcome the common numerical inaccuracy in voxel-based thickness computations due to the limited resolution of 3D grid.

Suppose M is a simplicial complex, and $g : |M| \rightarrow R^3$ a function that embeds |M| inR3, then (M, g) is called a mesh. For a 3-simplex, it is a tetrahedral mesh, T_e, and for a 2-simplex, it is a triangular mesh, T_r. Clearly, the boundary of a tetrahedral mesh is a triangular mesh, $T_r = \partial T_e$.

Definition 1. (Function Space).

All piecewise linear functions defined on M form a linear space, denoted by $C^{PL}(M)$.

Definition 2. (Inner Product).

Suppose a set of string constants k(u, v) are assigned, then the inner product on $C^{PL}(M)$ is defined as the quadratic form:

$$< f,g >= \frac{1}{2} \sum_{\{u,v\} \in K} k(u,v)(f(u) - f(v))(g(u) - g(v))$$ (3)

The energy is defined as the norm on $C^{PL}(M)$.

Definition 3. (String Energy).

Suppose $f \in C^{PL}(M)$, the string energy is defined as:

$$< f,g >= \frac{1}{2} \sum_{\{u,v\} \in K} k(u,v) \| f(u) - f(v) \|^2$$ (4)

By changing the string constants k(u, v) in the energy formula, we can define different string energies. Figure 4 shows the dihedral angle θ and edge l, to which the edge $[P_1, P_4]$ is against in the given tetrahedron. Based on it, we can define the discrete harmonic energy.
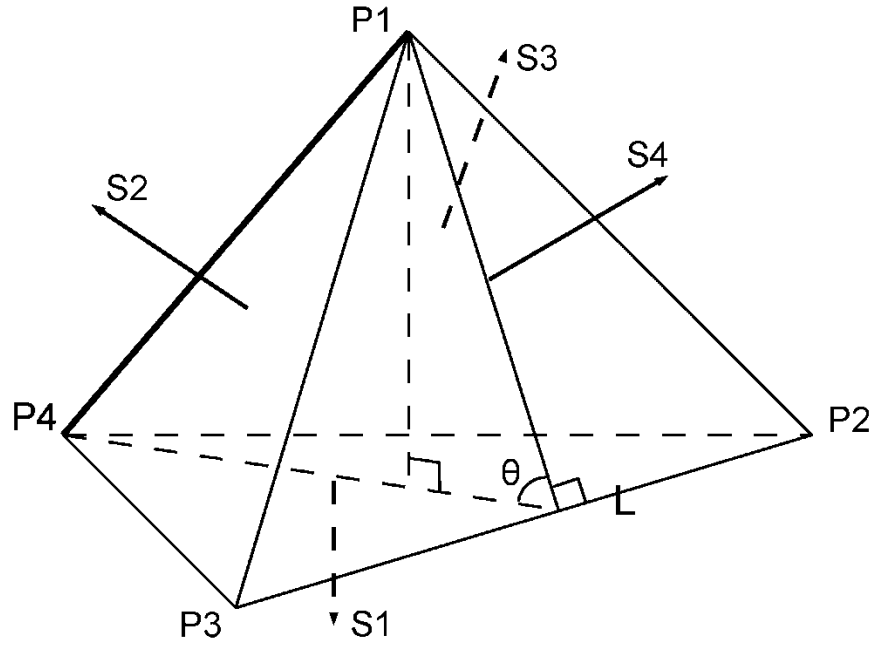
Figure 4. Illustration of a tetrahedron

Definition 4. (harmonic Energy (Wang et al., 2004a)).

Suppose for edge {u, v}, it is shared by n tetrahedrons. In each tetrahedron, there

is an edge which does not intersect with {u, v}, e.g. edge L in Figure 4. We call this

edge is against to {u, v} in this tetrahedron. Thus edge {u, v} is against to a total of

n edges, l_i, i = 1 … n, in these n tetrahedrons. Similarly, there is a dihedral angle

which is associated with L, e.g. θ in Figure 4. We call this dihedral angle θ is against

to edge {u, v} as well. So edge {u, v} is against to a total of n dihedral angles, θ_i, i

= 1 … n, in these n tetrahedron. Define the parameters

$$k_{u,v} = \frac{1}{12} \sum_{i=1}^{n} l_i cot(\theta_i) \tag{5}$$

Where l_i, i = 1 … n, is the lengths of the edges to which edge {u, v} is against in the

domain manifold M. The string energy obtained is called the harmonic energy.

The string energy is always a quadratic form. By carefully choosing the string coefficients, we can make sure that the quadratic form is positive definite. This will guarantee the convergence of the optimization process.

Definition 5. (Discrete Volumetric Laplace Operator).

The piecewise Laplacian is the linear operator $\Delta_{PL}: C^{PL}(M) \rightarrow C^{PL}(M)$ on the space of piecewise linear functions on M, defined by the formula

$$\Delta_{PL}(f) = \sum_{\{u,v\} \in M} k(u,v)(f(v) - f(u)) \tag{6}$$

If f minimizes the string energy, then f satisfies the condition

$$\Delta_{PL}(f) = 0$$

Suppose M_1, M_2 are two meshes and the map $\vec{f}: M_1 \rightarrow M_2$, is a map from M_1 to R^3.

Definition 6. (Harmonic Energy of Maps).

For a map $\vec{f}: M_1 \rightarrow R^3, \vec{f} = (f_1, f_2, f_3)$, we define the energy as the norm of $\vec{f}$:

$$E(\vec{f}) = \|\vec{f}\|^2 = \sum_{i=1}^{3} \|f_i\|^2 \tag{7}$$

The Laplacian is defined in a similar way.

Definition 7. (Laplace Operator).

For a map $\vec{f}: M_1 \rightarrow R^3$, the piecewise Laplacian of $\vec{f}$ if

$$\Delta_{PL}\vec{f} = (\Delta_{PL}f_1, \Delta_{PL}f_2, \Delta_{PL}f_3) \tag{8}$$

A map $\vec{f}: M_1 \rightarrow M_2$ is harmonic, if and only if it has a normal component, and the tangential component is zero.

$$\Delta_{PL}(\vec{f}) = (\Delta_{PL}\vec{f})^{\perp} \tag{9}$$

13

Definition 8. (Conventional Harmonic Energy (Schoen and Yau, 1997)).

Suppose f : M → R is a function defined on the mesh, the conventional harmonic

energy is defined as

$$E(f) = \int_M |\nabla_f|^2 d\sigma \qquad (10)$$

where dσ is the volume element of the 3 manifold and |∇f| is the gradient of the

function. A harmonic function is a harmonic map from M to R, therefore a harmonic

function has the property, e.g. Equation 1

$$\Delta f = 0$$

The following theorem provides the foundation for our work.

Proposition 1.

The discrete harmonic energy (Definition 4) and the conventional harmonic energy

(Definition 8) are consistent.

The detailed proof is given in the Appendix. The consistency between the

conventional harmonic energy and discrete harmonic energy opens a new avenue for

us to compute the harmonic map with the tetrahedral mesh. In the classical finite

element literature, it has been proven that discrete solutions to the discrete Laplace

equation converge to the smooth solution when the tetrahedral meshes are

subdivided to the limit. With the discrete volumetric operator (Definition 5), we can

conveniently compute the harmonic field with the tetrahedral meshes.

Harmonic Field Computation

Similar to our prior work on surface holomorphic 1-form computation (Wang

et al., 2011), one can compute the volumetric harmonic field by solving a linear

system defined with the Laplacian matrix. Here is the explanation of some key steps.

For the details and convergence of the linear systems, the readers are referred to

the rich harmonic map and spectral analysis literature, e.g. (Schoen and Yau, 1997; Coifman et al., 2005).

Definition 9.

Given a tetrahedral mesh, the graph weight matrix is defined as

$$S_{u,v} = \begin{cases} k_{u,v} & \exists e_{u,v} \\ 0 & \neg\exists e_{u,v} \end{cases}$$

where $k_{u,v}$ is defined in Definition 5. Clearly, S is a sparse matrix and can be decomposed as

$$S = \begin{pmatrix} W_{VV} & W_{V\partial V} \\ W_{\partial VV} & W_{\partial V\partial V} \end{pmatrix}$$

where V and ∂V represent the set of internal vertices and boundary vertices, respectively.

Definition 10.

Under Dirichlet boundary conditions, the Laplacian matrix is

$$L_p = D_{VV} + D_{V\partial V} - S_{VV},$$

where the diagonal matrix $DV \partial V = diag(S_{V\partial V}e_i)$, e_i is the i-th column vector in an identity matrix, i.e., $(D_{V\partial V})_{ii}$ = the sum of i-th row in $W_{V\partial V}$.

With the discrete Laplacian operator definition, we compute the harmonic field with Dirichlet boundary conditions,

$$L_p x = c \qquad\qquad (11)$$

where x is a |u| × 1 vector (|u| is the number of internal vertices). Note that x only contains unknown function values on internal vertices, i.e. W_{VV}, as shown in the definition of L_p; and the constant vector c is computed by

$$c_u = f_l^T W_{\partial VV} = \sum_{[u,w]\in M} f_l k_{v,w}$$

where f_l is the specified function value on boundary vertices.

Thickness Profile Generation

Equation 11 is the discretized version of Equation 2. After computing the harmonic field f by solving x for internal vertices in Equation 11, we can compute the streamlines to connect the two surfaces (Jones et al., 2000; Adamson et al., 2011). Computationally, we construct a streamline as a parametric curves u(s) with arc length parameter s. The thickness is defined as the total arc length of the streamline that traverses the CC from superior to inferior (or, alternatively, from inferior to superior) patches. Formally, we solve the following ordinary differential equation to construct the streamlines:

$$\begin{cases} u'(s) = \pm \dfrac{\nabla f(u(s))}{|\nabla f(u(s))|} \\ u(0) = x \end{cases} \tag{12}$$

where x is a point on the stating surface patch and the streamline stops when it intersects the other surface patch. u' takes different sign based on the starting surface patch. Solving for Equation 2 using B_0 as either the superior or inferior surface, and B_1 as the other surface, we can compute the thickness at each point on superior and inferior surfaces, respectively.

MULTIVARIATE MORPHOMETRIC ANALYSIS

Algorithm 1 illustrates the algorithm pipeline of our multivariate morphometry computation. In the following, we explain each step in detail.

1.   Tetrahedral mesh and triangular mesh generation;

2.   Surface registration and surface decomposition;

3.   Callosal thickness computation;

4.   Multivariate morphometry feature computation.

Algorithm 1. Multivariate Morphometry of 3D Corpus Callosum.

Input: Binary image of segmented corpus callosum

Output: Morphometry features for each boundary vertex, including thickness and deformation tensors.

1.   Build tetrahedral mesh from the binary image; build triangular mesh by computing the boundary of the tetrahedral mesh;

2.   Register surfaces via holomorphic 1-form method (Wang et al., 2011); decompose a surface into superior and inferior patches by tracing iso-parametric curves;

3.   Compute callosal thickness using the harmonic field;

4.   Compute deformation tensors; construct the multivariate morphometry features by combining mTBM and thickness features.

Mesh Generation

Our meshes are generated by an adaptively sized tetrahedral mesh modeling method (Lederman et al., 2011). The method produces meshes conforming to the voxelized regions in the image by minimizing an energy function consisting of a smoothing term, a fidelity term and an elasticity term. Figure 1(a) shows the binary

image of a segmented Corpus Callosum and (b) shows its tetrahedral mesh. The

boundary of the tetrahedral mesh gives a surface triangular mesh for the callosal

surface (Figure 1(c)).

Surface Registration and Decomposition

The goal of this step is to register CC surfaces across subjects and

consistently decompose them into two pieces of surface patches for thickness

analysis. Given the long and thin structure of a CC surface, existing area-preserving

spherical mapping based subcortical algorithms (Styner et al., 2005a) may produce

much distortion. For an accurate surface registration and decomposition, we adopt

our holomorphic 1-form based method to compute a constrained harmonic map

between CC surfaces (Wang et al., 2011).

First, given a callosal surface, we label two consistent landmark curves at the

caudal and rostral endpoints. They are biologically valid and consistent landmarks

across subjects as shown in Figure 5(a) (blue lines). We call this process topological

optimization. Given the callosal horizontal tube-like shape, these landmarks curves

can be automatically detected by checking the extreme points along the first

principal direction of the geometric moments of the surface. Secondly, we

conformally map the callosal surface onto a rectangular planar domain with a

holomorphic 1-form based conformal parameterization algorithm as in (Wang et al.,

2011). Specifically, by computing the exact harmonic one-form (Figure 5 (b)), its

conjugate one-form (Figure 5 (c)), and canonical holomorphic one-form (Figure 5

(d)), we compute the conformal parameterization of callosal surface. Figure 5(d)

illustrates the conformal parameterization by texture mapping the checkerboard back
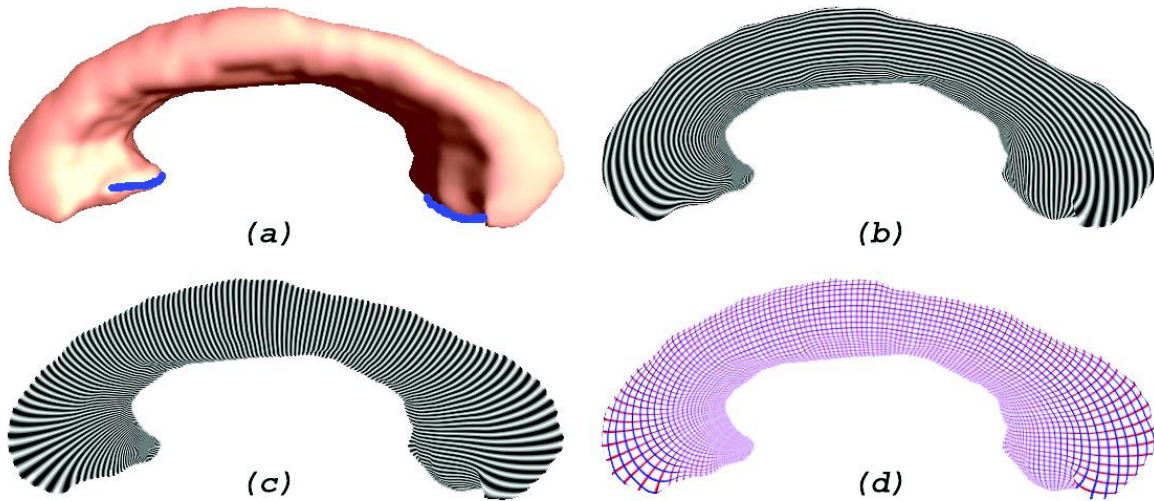
to the surface.

Figure 5. Illustration of callosal surface conformal parameterization

Figure 5 shows the callosal surface conformal parameterization via holomorphic one-forms. (a) Topology change. Two cuts were made on each callosal surface extreme point. (b) One computed exact harmonic one-form, which is visualized by integrating the one-form on the open boundary surface. (c) Conjugate one-form of the one-form in (b). It is locally perpendicular to the one-form in (b). (d) The canonical holomorphic one-form, which induces a conformal parameterization from callosal surface to the Euclidean domain. The conformality is visualized by texture mapping of a checkerboard image where the planar parameterization coordinates are used as the texture coordinates. All the right angles in the texture are preserved on the brain surface.

On the parameterized surfaces, we generate two iso-parametric curves which pass the extreme points on two lateral sides. By cutting along these two curves and removing their attached triangles (also the tetrahedron in the tetrahedral mesh), we produce superior and inferior surface patches, which are used for the callosal surface registration and thickness computation
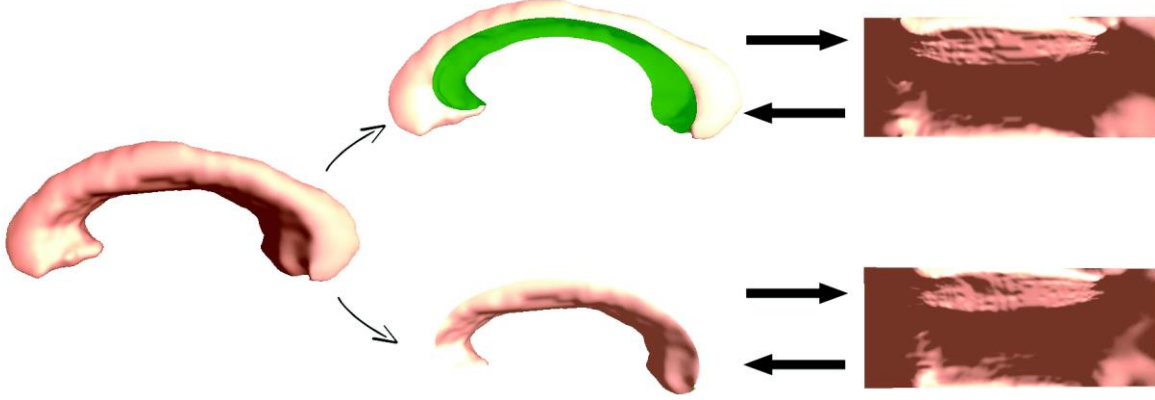
19

Figure 6. Illustration of callosal surface registration

Figure 6 illustrates the surface registration process. Holomorphic one-forms are used to induce two iso-u curves on the curvilinear coordinates which cut the callosal surface into two pieces, superior part and inferior part. Each piece of the callosal surface is conformally mapped to a rectangle in the parameter domain. The shading effect on the parameter space is generated by rendering the original 3D surface with the surface normal directions on each point. The planar parameterization results are used for surface registration and morphometric analysis.

Finally, given two callosal surfaces (either superior patch or inferior patch) S_1 and S_2 and their parameterizations, $\tau_1 : S_1 \rightarrow R^2$ and $\tau_2 : S_2 \rightarrow R^2$, we find a harmonic map $\tau : R^2 \rightarrow R^2$ between the parameter domains, such that:

$$\tau \circ \tau_1(S_1) = \tau_2(S_2), \ \tau \circ \tau_1(\partial S_1) = \tau_2(\partial S_2), \ \Delta\tau = 0.$$

Then the map ϕ can be obtained by $\phi = \tau_1 \circ \tau \circ \tau_2^{-1}$

Since τ is a harmonic map, and τ_1 and τ_2 are conformal maps, the resulting ϕ is a harmonic map. When landmark curves need to be matched, such as the boundaries of each component of the ventricles, we guarantee the matching of both ends of the curves. We also match the rest of the curves in 3D based on unit speed parameterizations of both curves.

Thickness Computation

After the surface is decomposed into superior and inferior patches, we apply

the tetrahedral mesh based callosal thickness algorithm to compute the callosal

thickness. The details of the algorithm are described in Chapter 3. After solving the

Laplace's equation, we build a harmonic field between two surface patches. On the

harmonic field, the level set of equal harmonic function values construct different
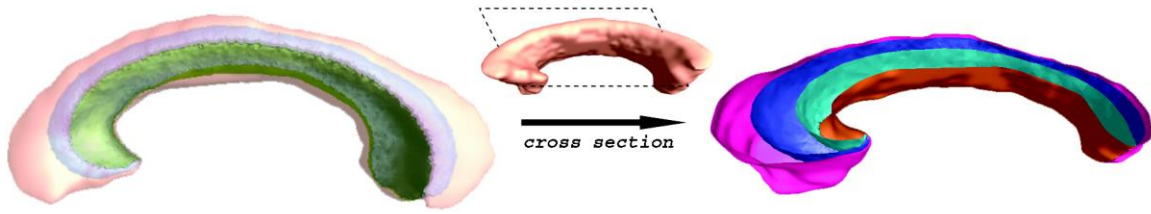
layers.

Figure 7. Illustration of the harmonic fields

Figure 7 shows an example of computed surface layers. Different color surface

represent surface level sets with equal function values. The left panel shows a

volumetric rendering. The right panel shows a zoomed-in result after a cut along the

sagittal direction. The stream lines are computed by tracing the normal directions of

the surface level set. Finally, the computed stream line lengths define the thickness

profile on the callosal surface.

Multivariate Morphometry Feature Computation

Our complete multivariate morphometry feature consists of deformation

tensors in log-Euclidean space and callosal thickness. Given two triangles, [V1, V2,

V3] and [W1, W2, W3], first, we isometrically embed them onto the plane R2; the

planar coordinates of the vertices of V_i, W_j are denoted using the same symbols V_i,

W_j. Then we explicitly compute the Jacobian matrix J,

$$J = [W3 - W1, W2 - W1][V3 - V1, V2 - V1]^{-1}$$

The deformation tensor can be defined as $S = (J^T J)^{0.5}$. Instead of analyzing

shape change based on the eigenvalues of the deformation tensor, a new family of

metrics, the "Log-Euclidean metrics" (Arsigny et al., 2006) is used in multivariate tensor-based morphometry (mTBM). This conversion makes computations on tensors easier to perform, as they are chosen such that the transformed values form a vector space, and statistical parameters can then be computed easily using the standard formulae for Euclidean spaces.

Similar to the practice in (Leporé et al., 2008; Shi et al., 2013a), we also linearly covary the multivariate statistics at each pixel with subject age and gender information. Let A represent one of the four statistic, and Acov is the new adjusted statistic. The Acov is computed by fitting the following general linear model to the data at each vertex:

$$A = \beta_0 + \beta_1 \times age + \beta_2 \times gender + \beta_3 \times diagnosis + error;$$

where β_i, i = 0, 1, 2, 3 are estimated regression coefficients at the specific vertex. Diagnosis is coded as a binary dummy variable (e.g. diagnosis = 0 (sighted control) and 1 (CB)) and gender is coded as a binary dummy variable (i.e. gender = 0 (male) and 1 (female)) so that Acov = $\beta_3 \times$ diagnosis + error = A $- \beta_0 - \beta_1 \times$ age $- \beta_2 \times$ gender. For the multivariate measures, the regression is computed separately for each channel.

The covaried statistics are used for a group difference study. For the group difference test, we run a permutation test with 5000 random assignments of subjects to groups to estimate the statistical significance (p-maps) in surface morphometry (Wang et al., 2011).

To compute group differences with multivariate morphometry features, we then apply Hotelling's T^2 test on sets of multivariate morphometry values. Given two groups of (n × 1)-dimensional vectors, S_i, i = 1, 2, p, T_j, j = 1, 2, q, we use the Mahalanobis distance M to measure the group mean difference,

$$M = \frac{N_S N_T}{N_S + N_T}(S - T)\sum^{-1}(S - T)$$

where N_S and N_T are the number of subjects in the two groups, S and T are the means of the two groups and Σ is the combined covariance matrix of the two groups (Leporé et al., 2008). Since the statistic M is univariate, our analysis does not introduce any bias because of the increase in the number of variables.

RESULT

Linking Morphometry and Clinical Characteristics

At each surface point, associations were assessed between multivariate statistics and clinical characteristics. Our method picked up strong group differences in both hippocampal atrophy and ventricular enlargement between diagnostic groups.
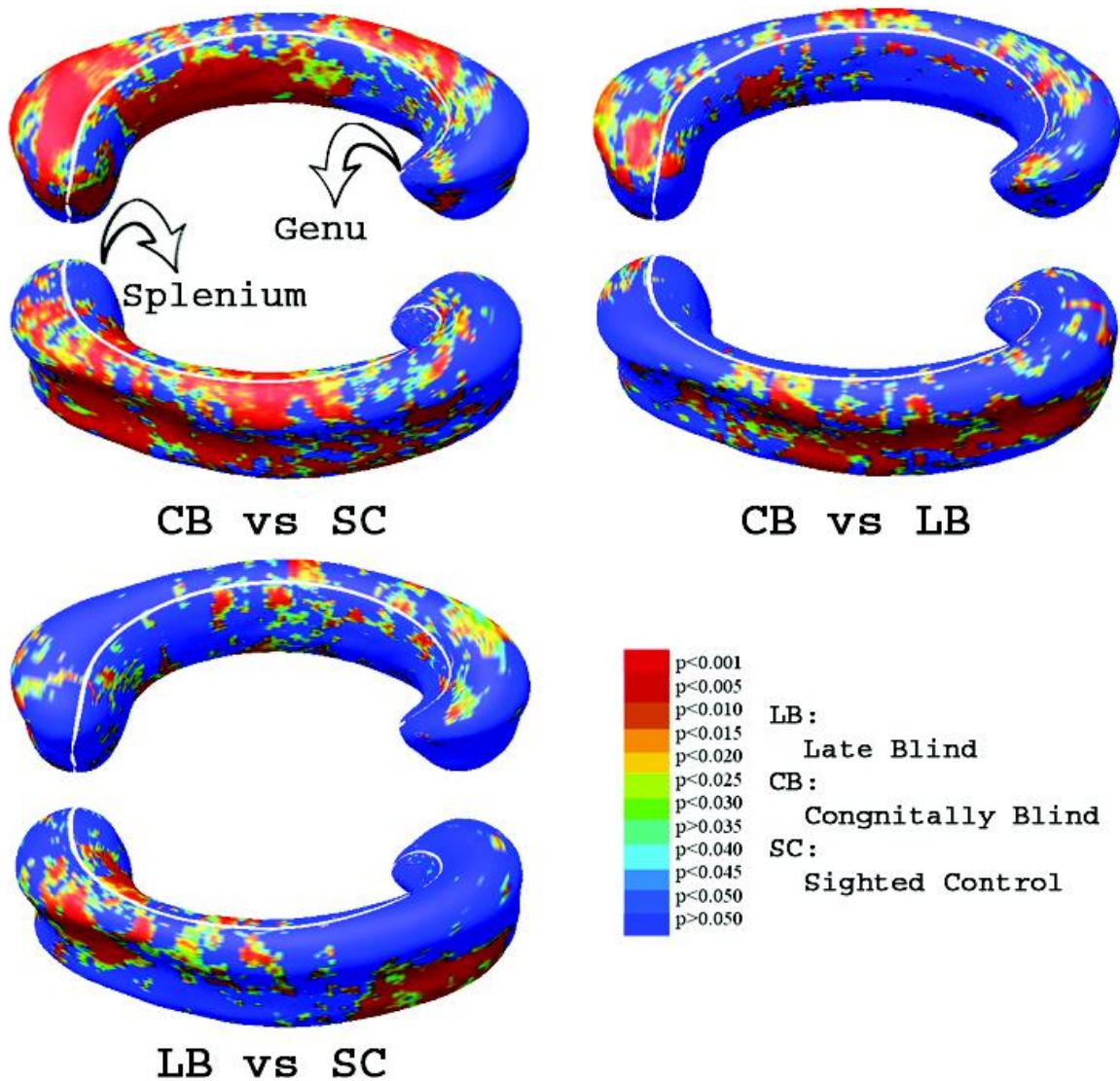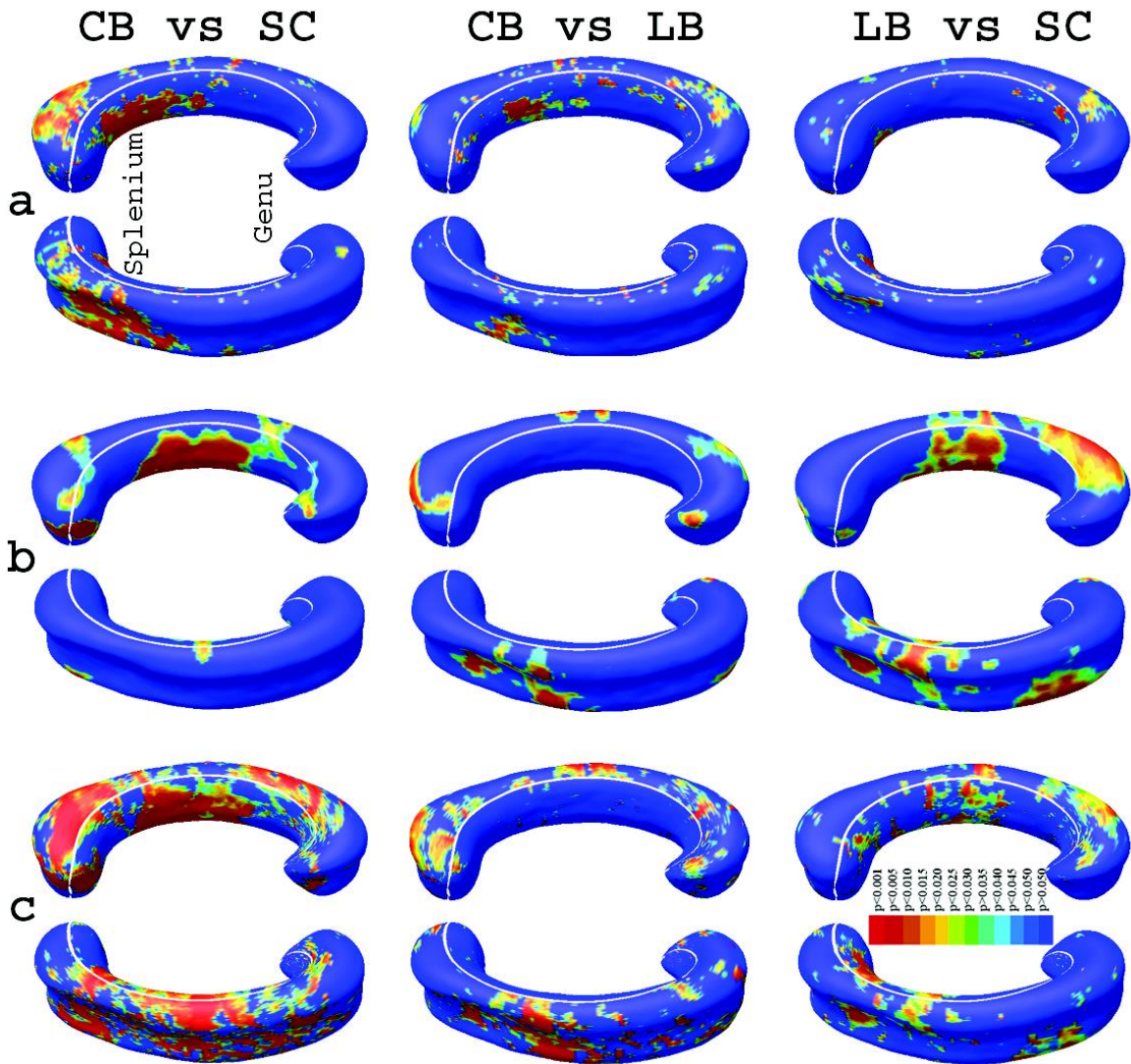

Figure 8. Comparison of p-maps with Thickness-mTBM

Figure 8 shows statistical maps of callosal morphometry and thickness changes in CB vs. SC, CB vs. LB and LB vs. SC.

It is worthwhile noting that our results are consistent with previous work (Leporé et al., 2010) and with the hypothesis that splenium regions should be affected in all blind groups, but more so in the CB. Our results are also consistent with another DTI tractography study (Yu et al., 2007), which found fractional anisotropy was significantly reduced in the splenium of CB subjects. The splenium is primarily composed of fibers connecting the visuospatial areas of the brain. The differences seen here may be due to reduced myelination of these fibers in the absence of visual input.

Other Morphometric Statistics

To explore whether our multivariate statistics provide extra power when combining thickness with mTBM, in each experiment, we also conducted three additional statistical tests using the thickness and different tensor-based statistics derived from the Jacobian matrix. The other statistics we studied are: (1) the thickness (THK) itself; (2) the determinant of Jacobian matrix (Davatzikos, 1996; Chung et al., 2008); and (3) the mTBM (Leporé et al., 2008; Wang et al., 2010). For statistics (1) and (2), we applied a Student's t-test to compute the group mean-difference at each surface point. In case (3) and for our new combined measure, we used Hotelling's T^2 statistics to compute the group mean-difference. In all sets of results, we detected significant areas around splenium areas for the combined measure. The CB also show significant changes in the body of the CC.

(a):THK   (b):TBM   (c):mTBM

LB:Late Blind   CB:Congnitally Blind   SC:Sighted Control

Figure 9. Comparison of p-maps with three statistics

In Figure 9, Non-blue colors show vertices with statistical differences, at the 0.05 level, uncorrected. The combined multivariate statistics outperforms all three individual statistics (the critical p-values for these maps are shown in Figure 10).

All group difference p-maps were corrected for multiple comparisons using the false discovery rate method (FDR) (Benjamini and Hochberg, 1995). The FDR method determines the critical p-value, which is the highest threshold p-value that

controls the FDR at the given threshold, e.g. 5%. To rank which clinical measures

were most strongly associated with callosal morphology, we created cumulative

distribution function (CDF) plots of the resulting uncorrected p-values. The critical p-

value, which is the highest non-zero point at which the CDF plot intersects the y =

20x line, represents the highest statistical threshold for which at most 5% false

positive are expected in the map. If there is no such intersection point (other than

the origin), there is no evidence to reject the null hypothesis. Also, steeper CDFs

show stronger effect sizes. FDR results are shown in Figure 10. All measures are

significant for the CB vs. controls, while only our new combined measure falls above

the y = 20x line in the case of LB vs. controls.
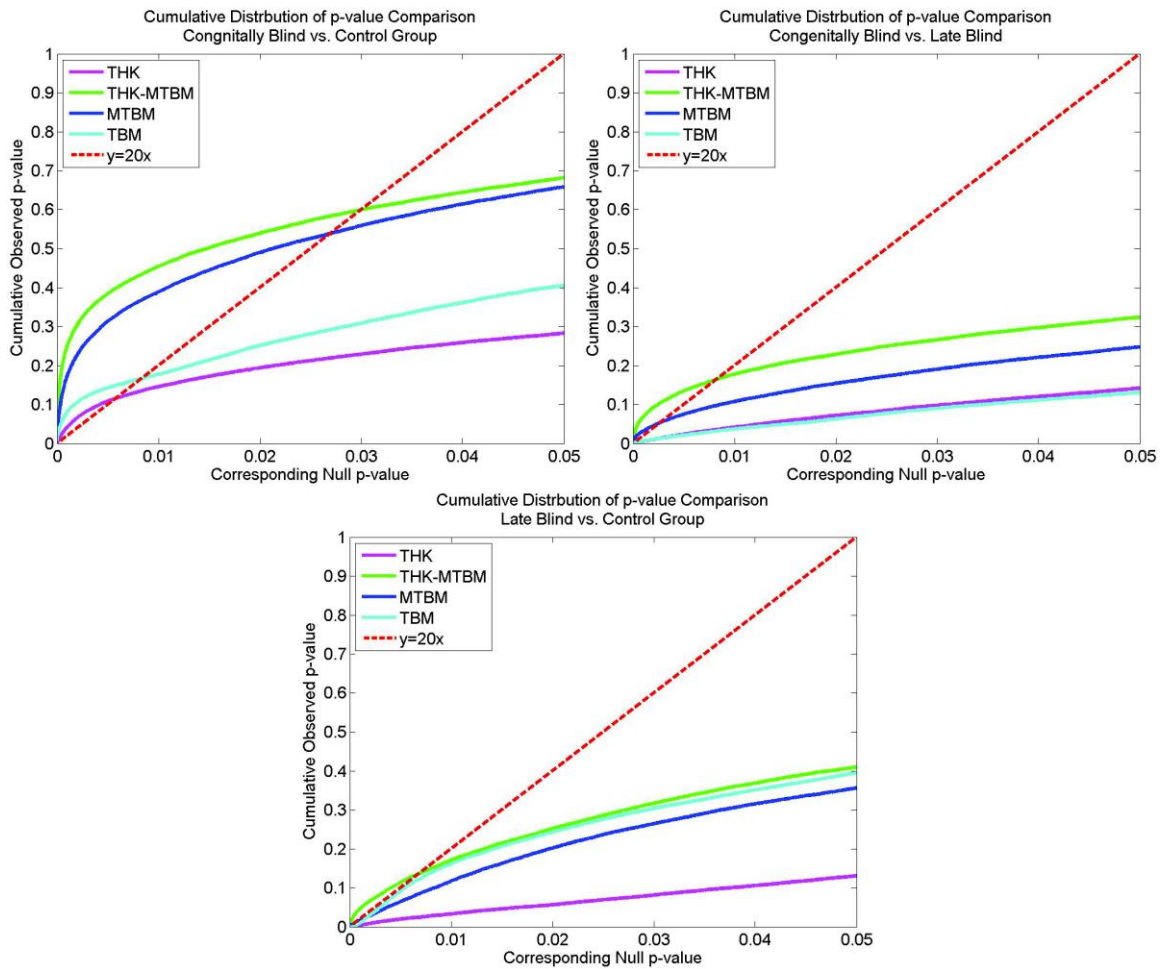

Figure 10. The cumulative distributions of the p-values

Figure 10 shows the cumulative distributions for difference detected between three diagnostic groups (CB, LB and SC) for all four statistics. The critical p-values are the intersection points of the curves and the y = 20x line. The new multivariate statistics achieved the highest critical p-values in all 3 comparisons.

DISCUSSION

There are three main contributions in this paper. First, we propose an efficient tetrahedral mesh based method to compute the harmonic field. Prior work on voxel-based brain thickness analysis (Jones et al., 2000; Adamson et al., 2011) relied on a three-dimensional cubic voxel grid to solve partial differential equations (PDE) in the potential field. However, due to the restrictions on the grid resolution which cannot precisely characterize the curved cortical surfaces in MR images, the measurement accuracy from this method is low and sensitive to noise. Our approach overcomes the defect of the limited grid resolution by adopting a high quality, adaptive tetrahedral mesh (Lederman et al., 2011) and a finite element based Laplacian operator (Wang et al., 2004a). Compared with prior work (Jones et al., 2000; Adamson et al., 2011), our PDE solving computation can achieve sub-voxel accuracy. Also because surfaces are easily computed from tetrahedral meshes, our method can be easily integrated with prior surface registration work (Wang et al., 2010, 2011, 2013c) to achieve a comprehensive morphometry study. Second, we propose a multivariate statistics by combining the callosal thickness computed from our new method and mTBM. Lastly, through multiple comparisons, we identify statistically significant areas on CC between the CB and LB groups. This discovery may help further our understanding of brain plasticity and in the long term; improve the effectiveness of rehabilitation techniques for blind individuals.

Our preliminary results on CB, LB and SC subjects are consistent with previous work and with the hypothesis that splenium regions should be affected in all blind groups, but more so in the CB. In addition, with our novel multivariate statistics, we found changes in the body of the CC in the LB group while no such difference was detected in (Leporé et al., 2010). In the late blind subjects, the process of myelination is relatively advanced, so that the structure of the corpus

29

callosum may not be that strongly influenced by the loss of visual perception. Our new discovery, generally consistent with this understanding, may provide additional insights to the myelination and cortical plasticity process. More importantly, these results also suggest that the newly proposed multivariate morphometry has more detection power in terms of effect size, likely because it captures callosal thickness and more directional and rotational information when measuring geometric differences.

The work reported here is related to ongoing research on the heat kernel and spectral analysis work. Recently, surface based heat kernel methods have been widely used in image shape analysis (Chung et al., 2005), classification (Bronstein and Bronstein, 2011), and registration (Sharma et al., 2012). Surface spectral analysis techniques are applied to surface registration (Lombaert et al., 2012), cortical surface reconstruction (Shi et al., 2010, 2013b) and automatic corpus callosum extraction on cortical surfaces (Lai et al., 2011). They all involve the Laplacian-Beltrami operator computation. However, 3D heat kernel methods are still rare in the medical image analysis field. Based on a prior development (Wang et al., 2004a), here we further show that the proposed discrete volumetric Laplacian operator can be adopted to compute the conventional harmonic energy. Besides the computational efficacy and efficiency, our method also takes numerous other advantages of the spectral analysis such as the measurement invariance of inelastic deformation and the robustness of the topological noise. We hope our work can lay down some of the theoretic foundation and attract some interest for further 3D heat kernel based method development in the neuroimaging field.

In the future, we will combine and correlate our multivariate statistical framework with other MRI imaging systems, such as cortical morphometry and diffusion tensor imaging (DTI) tractography, to advance our understanding of

blindness and improve the effectiveness of rehabilitation techniques and quality of life for blind individuals.

REFERENCES

Adamson, C.L., Wood, A.G., Chen, J., Barton, S., Reutens, D.C., Pantelis, C., Velakoulis, D., Walterfang, M. (2011). Thickness profile generation for the corpus callosum using Laplace's equation. *Human Brain Mapping, 32*, 2131–2140.

Amedi, A., Raz, N., Pianka, P., Malach, R., Zohary, E. (2003). Early 'visual' cortex activation correlates with superior verbal memory performance in the blind. *Nature Neuroscience, 6*, 758–766.

Arsigny, V., Fillard, P., Pennec, X., Ayache, N. (2006). Log-Euclidean metrics for fast and simple calculus on diffusion tensors. *Magnetic Resonance in Medicine, 56*, 411–421.

Bedny, M., Pascual-Leone, A., Dodell-Feder, D., Fedorenko, E., Saxe, R. (2011). Language processing in the occipital cortex of congenitally blind adults. *Proceedings of the National Academy of Sciences of the United States of America, 108*, 4429–4434.

Belluck, P. (2013). Burst of technology helps blind to see. *New York Times.*

Benjamini, Y., Hochberg, Y. (1995). Controlling the False Discovery Rate: A Practical and Powerful Approach to Multiple Testing. *Journal of the Royal Statistical Society. Series B (Methodological) 57*, 289–300. http://dx.doi.org/10.2307/2346101, doi:10.2307/2346101.

Bock, A.S., Saenz, M., Tungaraza, R., Boynton, G.M., Bridge, H., Fine, I. (2013). Visual callosal topography in the absence of retinal input. *Neuroimage, 81C*, 325–334.

Bronstein, M.M., Bronstein, A.M. (2011). Shape recognition with spectral distances. *IEEE Trans Pattern Anal Mach Intell, 33*, 1065–1071.

Chung, M.K., Dalton, K.M., Davidson, R.J. (2008). Tensor-based cortical surface morphometry via weighted spherical harmonic representation. *IEEE Trans Med Imaging, 27*, 1143–1151.

Chung, M.K., Robbins, S.M., Dalton, K.M., Davidson, R.J., Alexander, A.L., Evans, A.C. (2005). Cortical thickness analysis in autism with heat kernel smoothing. *NeuroImage, 25*, 1256–1265.

Chung, M.K., Worsley, K.J., Paus, T., Cherif, C., Collins, D.L., Giedd, J.N., Rapoport, J.L., Evans, A.C. (2001). A unified statistical approach to deformation-based morphometry. *Neuroimage, 14*, 595–606.

Coifman, R.R., Lafon, S., Lee, A.B., Maggioni, M., Nadler, B., Warner, F., Zucker, S.W. (2005). Geometric diffusions as a tool for harmonic analysis and structure definition of data: diffusion maps. *Proceedings of the National Academy of Sciences of the United States of America, 102*, 7426–7431.

Collignon, O., Lassonde, M., Leporé, F., Bastien, D., Veraart, C. (2007). Functional cerebral reorganization for auditory spatial processing and auditory substitution of vision in early blind subjects. Cerebral Cortex, *17*, 457–465.

Davatzikos, C. (1996). Spatial normalization of 3D brain images using deformable models. *J Comput Assist Tomogr, 20*, 656–665.

Di Paola, M., Luders, E., Cherubini, A., Sanchez-Castaneda, C., Thompson, P.M., Toga, A.W., Caltagirone, C., Orobello, S., Elifani, F., Squitieri, F., Sabatini, U. (2012). Multi- modal MRI analysis of the corpus callosum reveals white matter differences in presymptomatic and early Huntington's disease. *Cerebral Cortex, 22*, 2858–2866.

Doucet, M.E., Bergeron, F., Lassonde, M., Ferron, P., Leporé, F. (2006). Cross-modal reorganization and speech perception in cochlear implant users. *Brain, 129*, 3376–3383.

Gougoux, F., Belin, P., Voss, P., Leporé, F., Lassonde, M., Zatorre, R.J. (2009). Voice perception in blind persons: a functional magnetic resonance imaging study. *Neuropsychologia, 47*, 2967–2974.

Herron, T.J., Kang, X., Woods, D.L. (2012). Automated measurement of the human corpus callosum using MRI. *Front Neuroinform, 6*, 25.

Hofer, S., Frahm, J. (2006). Topography of the human corpus callosum revisited– comprehensive fiber tractography using diffusion tensor magnetic resonance imaging. *Neuroimage, 32*, 989–994.

Hua, X., Leow, A.D., Levitt, J.G., Caplan, R., Thompson, P.M., Toga, A.W. (2009). Detecting brain growth patterns in normal children using tensor-based morphometry. *Human Brain Mapping, 30*, 209–219.

Hutton, C., De Vita, E., Ashburner, J., Deichmann, R., Turner, R. (2008). Voxel-based cortical thickness measurements in MRI. *Neuroimage, 40*, 1701–1710.

Jenkinson, M., Smith, S. (2001). A global optimization method for robust affine registration of brain images. *Med Image Anal, 5*, 143–156.

Jiang, J., Zhu, W., Shi, F., Liu, Y., Li, J., Qin, W., Li, K., Yu, C., Jiang, T. (2009). Thick visual cortex in the early blind. *The Journal of Neuroscience, 29*, 2205–2211.

Jones, S.E., Buchbinder, B.R., Aharon, I. (2000). Three-dimensional mapping of cortical thickness using Laplace's equation. *Human Brain Mapping, 11*, 12–32.

Lai, R., Shi, Y., Sicotte, N., Toga, A. (2011). Automated corpus callosum extraction via laplace-beltrami nodal parcellation and intrinsic geodesic curvature flows on surfaces. *Computer Vision (ICCV), 2011 IEEE International Conference on, pp*. 2034–2040.

Lederman, C., Joshi, A., Dinov, I., Vese, L., Toga, A., Van Horn, J.D. (2011). The generation of tetrahedral mesh models for neuroanatomical MRI. *Neuroimage, 55*, 153–164.

Leporé, N., Brun, C., Chou, Y.Y., Chiang, M.C., Dutton, R.A., Hayashi, K.M., Luders, E., Lopez, O.L., Aizenstein, H.J., Toga, A.W., Becker, J.T., Thompson, P.M. (2008). Generalized tensor-based morphometry of HIV/AIDS using multivariate statistics on deformation tensors. *IEEE Transactions on Medical Imaging, 27*, 129–141.

Leporé, N., Shi, Y., Leporé, F., Fortin, M., Voss, P., Chou, Y.Y., Lord, C., Lassonde, M., Dinov, I.D., Toga, A.W., Thompson, P.M. (2009). Pattern of hippocampal shape and volume differences in blind subjects. *Neuroimage, 46*, 949–957.

Leporé, N., Voss, P., Leporé, F., Chou, Y.Y., Fortin, M., Gougoux, F., Lee, A.D., Brun, C., Lassonde, M., Madsen, S.K., Toga, A.W., Thompson, P.M. (2010). Brain structure changes visualized in early- and late-onset blind subjects. *Neuroimage, 49*, 134–140.

Li, B., Li, X., Wang, K., Qin, H. (2013). Surface mesh to volumetric spline conversion with generalized polycubes. *Visualization and Computer Graphics, IEEE Transactions on, 19*, 1539–1551.

Li, X., Guo, X., Wang, H., He, Y., Gu, X., Qin, H. (2007). Harmonic volumetric mapping for solid modeling applications. *Proceedings of the 2007 ACM symposium on Solid and physical modeling, ACM, New York, NY, USA*, 109–120.

Li, X., Xu, H., Wan, S., Yin, Z., Yu, W. (2010). Feature-aligned harmonic volumetric mapping using MFS. *Computers & Graphics, 34*, 242–251.

Lombaert, H., Grady, L., Polimeni, J.R., Cheriet, F. (2012). FOCUSR: Feature Oriented Correspondence using Spectral Regularization - A Method for Accurate Surface Matching. *IEEE Trans Pattern Anal Mach Intell*.

Luders, E., Narr, K.L., Zaidel, E., Thompson, P.M., Jancke, L., Toga, A.W. (2006). Parasagittal asymmetries of the corpus callosum. *Cerebral Cortex, 16*, 346–354.

Luders, E., Thompson, P.M., Toga, A.W. (2010). The development of the corpus callosum in the healthy human brain. *The Journal of Neuroscience, 30*, 10985–10990.

Pai, D., Soltanian-Zadeh, H., Hua, J. (2011). Evaluation of fiber bundles across subjects through brain mapping and registration of diffusion tensor data. *Neuroimage 54 Suppl, 1*, S165–175.

Paillé, G.P., Poulin, P. (2012). As-conformal-as-possible discrete volumetric mapping. *Computers & Graphics, 36*, 427–433.

Park, H.J., Lee, J.D., Kim, E.Y., Park, B., Oh, M.K., Lee, S., Kim, J.J. (2009). Morphological alterations in the congenital blind based on the analysis of cortical thickness and surface area. *Neuroimage, 47*, 98–106.

Ricciardi, E., Pietrini, P. (2011). New light from the dark: what blindness can teach us about brain function. *Current Opinion in Neurology, 24*, 357–363.

Schmitt, O., Bohme, M. (2002). A robust trans-cortical profile scanner for generating 2-d traverses in histological sections of richly curved cortical courses. *Neuroimage, 16*, 1103–1119.

Schoen, R., Yau, S.T. (1997). Lectures on Harmonic Maps. *International Press*.

Sharma, A., Horaud, R.P., Mateus, D. (2012). 3D shape registration using spectral graph embedding and probabilistic matching. *Image Processing and Analyzing With Graphs: Theory and Practice*, 441–474 http://perception.inrialpes.fr/Publications/2012/SHM12.

Shi, J., Wang, Y., Ceschin, R., An, X., Lao, Y., Vanderbilt, D., Nelson, M.D., Thompson, P.M., Panigrahy, A., Leporé, N. (2013a). A Multivariate Surface-Based Analysis of the Putamen in Premature Newborns: *Regional Differences within the Ventral Striatum. PLoS ONE, 8,* e66736.

Shi, Y., Lai, R., Morra, J.H., Dinov, I., Thompson, P.M., Toga, A.W. (2010). Robust surface reconstruction via Laplace-Beltrami Eigen-projection and boundary deformation. *IEEE Trans Med Imaging, 29*, 2009–2022.

Shi, Y., Lai, R., Toga, A.W. (2013b). Cortical surface reconstruction via unified Reeb analysis of geometric and topological outliers in magnetic resonance images. *IEEE Trans Med Imaging, 32*, 511–530.

Sieving, P.A., Caruso, R.C., Tao, W., Coleman, H.R., Thompson, D.J., Fullmer, K.R., Bush, R.A. (2006). Ciliary neurotrophic factor (CNTF) for human retinal degeneration: phase I trial of CNTF delivered by encapsulated cell intraocular implants. *Proceedings of the National Academy of Sciences of the United States of America, 103*, 3896–3901.

Styner, M., Lieberman, J.A., McClure, R.K., Weinberger, D.R., Jones, D.W., Gerig, G. (2005). Morphometric analysis of lateral ventricles in schizophrenia and healthy controls regarding genetic and disease-specific factors. *Current Opinion in Neurology, 102*, 4872–4877.

Styner, M.A., Oguz, I., Smith, R.G., Cascio, C., Jomier, M. (2005). Corpus callosum subdivision based on a probabilistic model of inter-hemispheric connectivity. *Med Image Comput Assist Interv, 8*, 765–772.

Tan, Y., Hua, J., Qin, H. (2010). Physically based modeling and simulation with dynamic spherical volumetric simplex splines. *Computer-Aided Design, 42*, 95–108.

Tepest, R., Jacobi, E., Gawronski, A., Krug, B., Moller-Hartmann, W., Lehnhardt, F.G., Vogeley, K. (2010). Corpus callosum size in adults with high-functioning autism and the relevance of gender. *Psychiatry Res, 183*, 38–43.

Voss, P., Lassonde, M., Gougoux, F., Fortin, M., Guillemot, J.P., Leporé, F. (2004). Early- and late-onset blind individuals show supra-normal auditory abilities in far-space. *Current Biology, 14*, 1734–1738.

Voss, P., Zatorre, R.J. (2012). Occipital cortical thickness predicts performance on pitch and musical tasks in blind individuals. *Cerebral Cortex, 22*, 2455–2465.

Wang, D., Qin, W., Liu, Y., Zhang, Y., Jiang, T., Yu, C. (2013). Altered white matter integrity in the congenital and late blind people. *Neural Plasticity, 2013*, 128236.

Wang, G., Li, J., Chen, J., Wang, L., Jiang, Z., Su, Q., Liu, Q., Ma, Y., Xu, L., Shi, J., Wang, Y. (2013). A heat kernel based cortical thickness estimation algorithm. *accepted by the 3rd MICCAI Workshop on Multimodal Brain Image Analysis (MBIA).*

Wang, K., Li, X., Li, B., Xu, H., Qin, H. (2012). Restricted trivariate polycube splines for volumetric data modeling. Visualization and Computer Graphics, *IEEE Transactions on, 18*, 703–716.

Wang, Y., Gu, X., Chan, T.F., Thompson, P.M., Yau, S.T. (2004a). Volumetric harmonic brain mapping, in: Biomedical Imaging: From Nano to Macro, 2004. ISBI 2004. *IEEE International Symposium on*, pp. 1275–1278.

Wang, Y., Gu, X., Yau, S.T. (2004b). Volumetric harmonic map. *Communications in Information and Systems, 3*, 191–202.

Wang, Y., Panigrahy, A., Shi, J., Ceschin, R., Nie, Z., Nelson, M.D., Leporé, N. (2012). 3D vs. 2D surface shape analysis of the corpus callosum in premature neonates, in: *MICCAI workshop on Paediatric and Perinatal Imaging*, Nice, France.

Wang, Y., Song, Y., Rajagopalan, P., An, T., Liu, K., Chou, Y.Y., Gutman, B., Toga, A.W., Thompson, P.M. (2011). Surface-based TBM boosts power to detect disease effects on the brain: An N=804 ADNI study. *Neuroimage, 56*, 1993–2010.

Wang, Y., Yuan, L., Shi, J., Greve, A., Ye, J., Toga, A.W., Reiss, A.L., Thompson, P.M. (2013c). Applying tensor-based morphometry to parametric surfaces can improve MRI-based disease diagnosis. *Neuroimage, 74*, 209–230.

Wang, Y., Zhang, J., Gutman, B., Chan, T.F., Becker, J.T., Aizenstein, H.J., Lopez, O.L., Tamburo, R.J., Toga, A.W., Thompson, P.M. (2010). Multivariate tensor-based morphometry on surfaces: application to mapping ventricular abnormalities in HIV/AIDS. *Neuroimage, 49*, 2141–2157.

Xu, H., Yu, W., Gu, S., Li, X. (2013). Biharmonic volumetric mapping using fundamental solutions. Visualization and Computer Graphics, *IEEE Transactions on, 19*, 787–798.

Yezzi, A.J., Prince, J.L. (2003). An Eulerian PDE approach for computing tissue thickness. *IEEE Trans Med Imaging, 22*, 1332–1339.

Yu, C., Shu, N., Li, J., Qin, W., Jiang, T., Li, K. (2007). Plasticity of the corticospinal tract in early blindness revealed by quantitative analysis of fractional anisotropy based on diffusion tensor tractography. *Neuroimage, 36*, 411–417.

Yushkevich, P.A., Piven, J., Hazlett, H.C., Smith, R.G., Ho, S., Gee, J.C., Gerig, G. (2006). User-guided 3D active contour segmentation of anatomical structures: significantly improved efficiency and reliability. *Neuroimage, 31*, 1116–1128.